Soft Matter

ARTICLE TYPE

Cite this: DOI: 00.0000/xxxxxxxxxx

Three-Dimensional Blueprinting of Molecular Patterns in Liquid Crystalline Polymers†

Mohsen Tabrizi,[a] J. Arul Clement,[a] Mahnoush Babaei,[b] Angel Martinez,[c] Junfeng Gao,[a] Taylor H. Ware,[d,e] and M. Ravi Shankar[a,*]

Received Date
Accepted Date

DOI: 00.0000/xxxxxxxxxx

Exploiting the interplay of anisotropic diamagnetic susceptibility of liquid crystalline monomers and site selective photopolymerization enables the fabrication of 3D freeforms with highly refined microstructures. Utilizing chain transfer agents in the mesogenic inks presents a pathway for broadly tuning the mechanical properties of liquid crystalline polymers and their response to stimuli. In particular, the combination of 1,4-benzenedimethanethiol and tetrabromomethane is shown to enable voxelated blueprinting of molecular order, while allowing for a modulation of the crosslink density and the mechanical properties. The formulation of these monomers allows for the resolution of the voxels to approach the limits set by the coherence lengths defined by the anchoring from surfaces. These compositions demonstrate the expected thermotropic responses while allowing for their functionalization with photochromic switches to elicit photomechanical responses. Actuation strains are shown to outstrip that accomplished with prior systems that did not access chain transfer agents to modulate the structure of the macromolecular network. Test cases of this system are shown to create freeform actuators that exploit the refined director patterns during high-resolution printing. These include topological defects, hierarchically-structured light responsive grippers, and biomimetic flyers whose flight dynamics can be actively modulated via irradiation with light.

1 Introduction

The compliance of soft actuators embodies an expansion of accessible degrees of freedom and finesse with which manipulation can be programmed, which are prohibitively complex with traditional, structurally stiff (hard) actuators and manipulators. Examples from the natural world (e.g., cephalopods) present an aspirational goal for engineered soft robots, which require the ability to voxelate actuation profiles at refined scales ($\ll$mm). Spatially resolved actuation strain and distortion is the key to exploiting the overall structural compliance for complex shape morphing, novel modes of motility and complex manipulation of payloads. Within this paradigm, erasing the distinction between the actuator and the suspensory structure by microstructurally designing active matter brings the vision of "the material becoming the machine" closer to reality[1].

Liquid crystal polymers (LCP) are distinguished by the tailorability of their molecular orientation (nematic director) with microstructural refinement that is only limited by the relative strength of the Frank elastic constant with respect to the anchoring presented by neighboring material elements[2]. Blueprinting voxels with resolutions at the scale of 10's μm is feasible, which unlocks highly non-linear, work-dense actuation in monolithic films[3].

Programmable morphing of 3D structures emerged when freeform fabrication assimilated the ability to spatiotemporally pattern the nematic director. Direct ink Writing (DIW) was developed to 3D print LCP[4–6]. Through the printing process, mesogenic oligomers were extruded within their nematic temperature window, where uniaxial molecular orientation is induced parallel to the printing direction. Shear at the nozzle drives the nematic alignment. Controlling the raster path during DIW enabled blueprinting of the nematic director in 3D structures. Shape morphing of the 3D printed shapes was used to organize manipu-

[a]Department of Industrial Engineering, Swanson School of Engineering, University of Pittsburgh, PA 15261, USA. E-mail: ravishm@pitt.edu
[b]Department of Aerospace Engineering & Engineering Mechanics, University of Texas at Austin, 2617 Wichita Street, C0600, Austin, TX 78712 USA. E-mail: mahnoushb@utexas.edu
[c]Department of Applied Physics and Materials Science, Northern Arizona University, Science Annex, 525 S Beaver St, Flagstaff, AZ 86011, USA. E-mail: Angel.Martinez@nau.edu
[d]Department of Biomedical Engineering, Texas A&M University, 101 Bizzell Street, College Station, TX 77843, USA.
[e]Department of Materials Science and Engineering., Texas A&M University, 209 Reed McDonald Building, College Station TX 77843, USA. E-mail: taylor.ware@tamu.edu
∗ Corresponding Author
† Electronic Supplementary Information (ESI) available

lation and motility through the sequential thermal actuation of a soft robot[7]. Embedding LCP with liquid metal (LM) enables electrical actuation of the structure; conductive LM-LCP composites produce the Joule heating which triggers the actuation[8]. This composite fabrication enabled multimaterial structures that offered both electrothermal and photothermal responsiveness[8]. Sub-voxel control over the material structure was enabled by DIW by extruding the LM that is coaxial to the LCP. The ability to deterministically innervate electrically conductive elements within the LCP allowed for nascent proprioceptive responses in 3D printed active matter[9]. Deposition-based methods enable freeform printing of complex geometries, but the molecular patterning is inextricably bound to the build/raster sequence[4–6,10–12]. Orthogonal control over the molecular order and the composition of the LCP freeform during printing is not feasible with DIW.

Photopolymerization in combination with orthogonal cues for controlling the nematic order expands the design complexity that can be encoded in 3D printed LCP. One approach utilized reorientable magnetic fields to encode the molecular order in mesogenic monomers, which was preserved using site-selective photopolymerization[13]. Superposition of electric fields with photopolymerization was used for voxel-by-voxel blueprinting of molecular order.[14,15]. Guo et al. applied two-photon polymerization technique to generate LCE freeforms. The alignment complexity was enhanced by fabricating microchannels on the walls[16] to modulate molecular order. While freeforms can be fabricated through this process, it is not possible to voxelate the response to stimuli in an indexable manner with spatial selectivity. This was extended to a pick-and-place strategy. LCE cubes with predefined nematic orientations were fabricated, which were manually assembled to create the final structure, element-by-element[17]. In addition, selective photopolymerization was used to 3D print LCP structures for applications in energy dissipation, where their molecular order was not central for its functionality[18]. Where alignment is desired, an array of alignment techniques have been explored in conjunction with photopolymerization. These include superposition of shear[19], anisotropic swelling[20], and mechanical loading[21].

Building on our prior work, we are driven by the premise that utilization of magnetic fields during spatially selective photopolymerization offers a versatile tool for 3D printing LCP[13]. In addition to decoupling the accretion of material voxels from the encoding of molecular order, this approach can offer potential superposition of surface cues, electric fields and mechanical stimuli. Magnetic fields drive alignment of nematogens through an orienting moment that acts through the volume of the monomeric ink. This bulk effect when superposed with near-surface alignment strategies, offers a combinatorially rich set of process designs to enable hierarchically patterned LCP.

Previous research has explored programming the molecular alignment in glassy LCNs[13] and side-chain LCP[22] using low-intensity magnetic fields (< 0.5 T). If magnetically programmable, main-chain LCPs become 3D printable, freeform morphing structures can be realized to produce strains $> 10\%$, while generating actuation stresses >100's of kPa. Modest strains and actuation work-densities that characterize the glassy and side-chain systems can be overcome.

Here, we functionalize mesogenic inks with chain transfer agents to assimilate the ability to magnetically align the nematic director, while enabling 3D printing of LCP. A composition space of such inks is identified where the mechanical properties can be broadly modulated and the responsiveness to actinic stimuli can be magnified. The ability to tune the macromolecular structure through monomer design allows for magnified strain responses to optical stimuli, which is nearly an order-of-magnitude greater than that possible with prior systems[13]. This is harnessed in functional, freeform devices that present shape morphing powered by light. This capability is exemplified by printing 3D-scanned maple samara using photoresponsive polymers. Illuminating the falling biomimetic seeds modulates the structure of the wing, which in turn controls the aerodynamics of their flight. Thus, a new motif for non-contact all-optical control of biomimetic passive flyers emerges, enabled by the ability to print photoresponsive freeform LCP.

2 Results and discussion

Figure 1a illustrates the components of the mesogenic inks that were examined in this study. A range of compositions was explored to characterize the effect of chain transfer agents on the crosslink density and the resulting responsiveness (Table 1). The ability to magnify photomechanical responses in 3D printable inks enabled the creation of active structures that can morph and adapt their functionalities.

Building on our previous study[13] we employed a voxel-by-voxel approach to blueprint the molecular orientation in 3D freeforms (Figure 1b). To initiate the process, the monomer mixture is introduced to the system at a temperature within the nematic phase in the gap between the window and build-plate (the build-gap). The mesogenic order was controlled independent of the material accretion by an external rotatable magnetic field (300 mT). The build-gap consists of a substrate on which the structure is printed. The mesogens in the monomer state can be reoriented (twisted in this case) by the magnetic field. However, this reorientation is a kinetic process. Typically, the achievement of molecular ordering occurs at the time scale of minutes. This was a function of the material composition and magnetic field strength. Once orientation was achieved, a digital micromirror device (DMD) was used for selective exposure, which induces crosslinking and results in a polymerized LCE voxel that inherits the nematic alignment (Figure 1c). The molecular alignment was preserved after polymerization, as evidenced by in-situ POM observations (Figure S1 in Supplementary Information†). After a layer was formed through the repetition of the reorientation-polymerization steps, the build-plate was lifted, separating the polymerized layer from the window. The 3D printing process was completed through layer-by-layer fabrication steps, and excess uncured monomer was removed by dissolving and washing with a solvent, followed by drying and post-curing.

Thiol chain extenders constitute flexible chains and are used to modulate the macromolecular structure and in some cases decrease crosslinking density through the two-step Michael-addition process[4]. However, this synthesis method cannot be adopted for

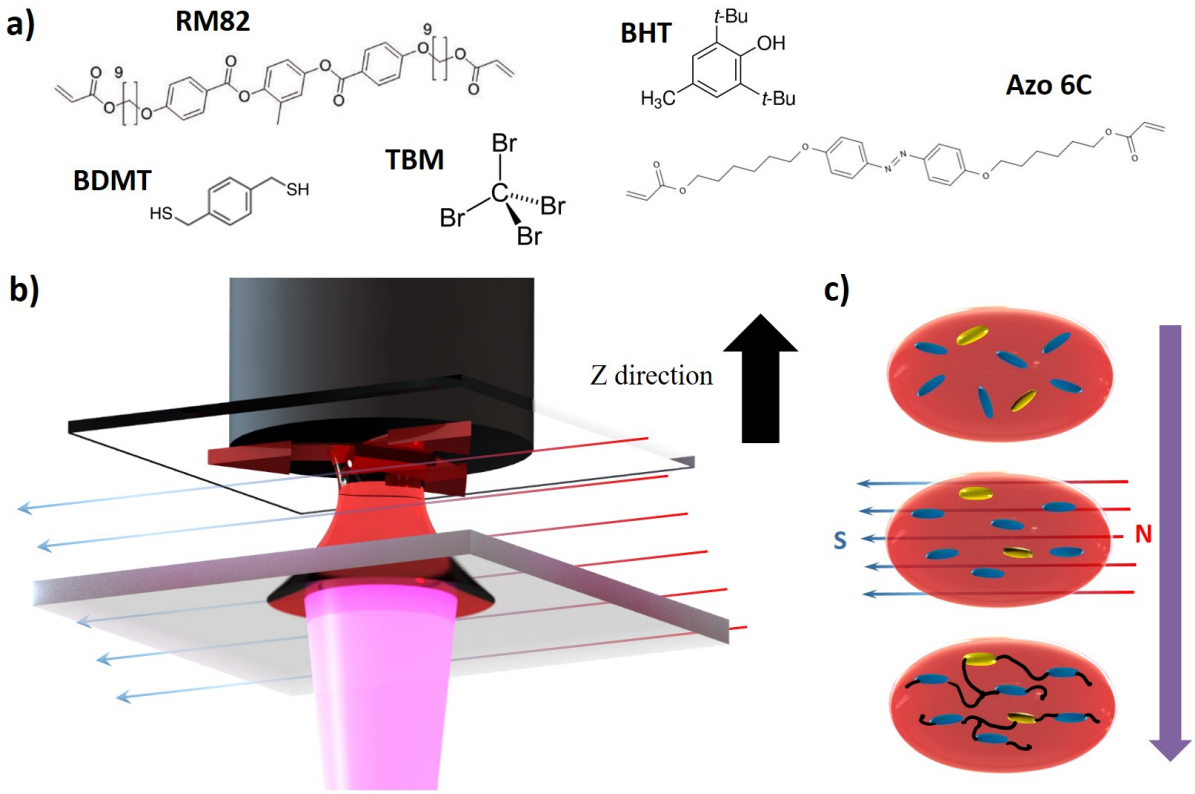

Fig. 1 a) Chemical structure of the LC monomers, azobenzene crosslinker, TBM chain transfer agent, BDMT, and BHT thermal inhibitor used in the mixture to print 3D freeforms. b) Schematic of the bottom-up 3D printing system. c) The underlying principle of molecular patterning. Mesogens within a voxel of material are aligned by a reorientable magnetic field. The orientation is subsequently locked-in through selective photopolymerization.

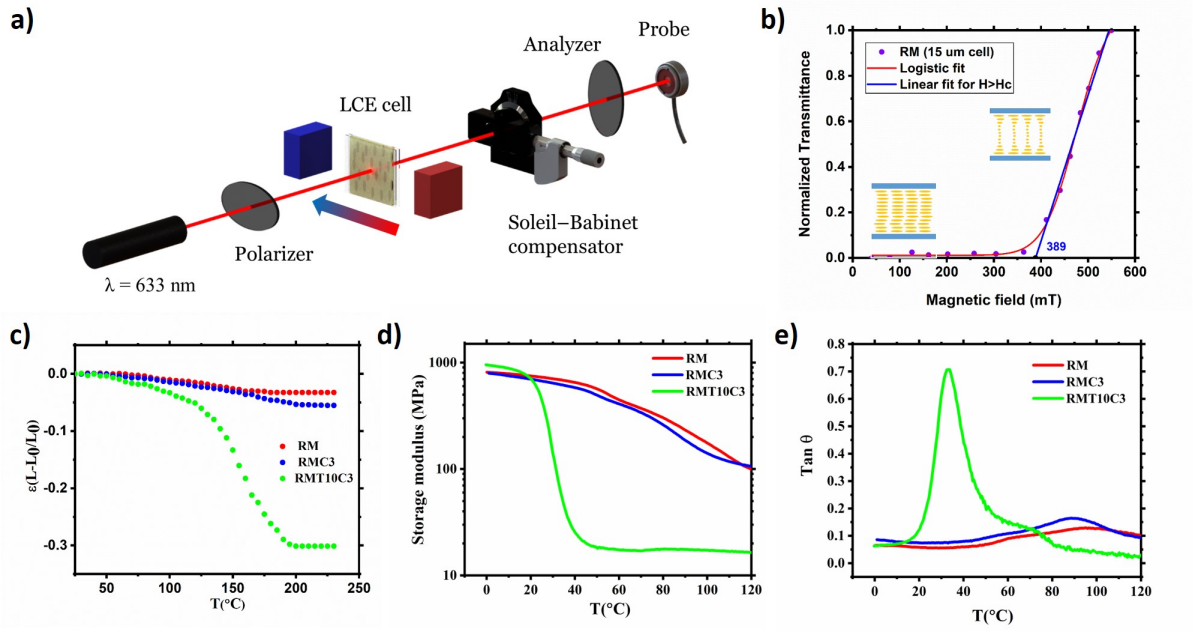

Fig. 2 a) Schematic of the critical field measurement. b) Normalized transmitted light intensity through a 15 μm cell filled with RM82 monomer in the nematic phase, versus applied magnetic field. Red line illustrates the fitted logistic curve, and the blue line was derived from linear fitting to estimate the magnetic field threshold. c) Thermal actuation strains in printed samples. d & e) DMA curves show change in material viscoelasticity by introducing TBM and BDMT to the composition.

the current printing process. Alignment of macromers formed by Michael Addition was not achievable using magnetic fields in the <0.5 T range (Figure S2). Godman et al.[23] proposed an alternative approach to decrease crosslinking density by utilizing a chain transfer agent (CTA). In their study, 1,4-benzenedimethanethiol (BDMT) was used as the CTA during the reaction process to terminate the chain and lower the crosslinking density. Unlike the two-step Michael-addition process, the mixture can be directly polymerized without oligomerization. We adopted this method by introducing BDMT and Tetrabromomethane (TBM) as CTAs to the mesogen monomer, RM82. TBM has been explored as a chain transfer agent that modulates the branching of a range of polymers and polymer networks[24–26]. The small molecular size was hypothesized to have a modest effect on the ability to magnetically align the mesophases by not significantly affecting the intermolecular coupling. We added the components individually and evaluated their impact on the mixture's ability to align under an external magnetic field.

Table 1 Monomer Mixtures of Various Compositions Explored in this Study

chemical composition	RM	RMC3	RMT10C3	RMZ4T10C3
RM82 [wt %]	99	96	84	80
BDMT [wt %]	0	0	10	10
Azo 6C [wt %]	0	0	0	4
TBM [wt %]	0	3	3	3
BHT [wt %]	1	1	3	3

For the LC material within a voxel, there exists a competition between the external magnetic field's orienting effect and the anchoring effect at the walls and voxel surfaces. Consider, a nematic LCE that fills a gap with a thickness of d. When an external magnetic field (H) is applied perpendicular to the surface-induced anchoring, the magnetic torque attempts to rotate and align the mesogens parallel to the field direction due to the mesogens' diamagnetic property. For a small H, the mesogens can stay undisturbed, maintaining the uniaxial alignment parallel to the easy axis of the wall. Once the magnetic field is increased beyond a certain threshold (critical field: H_c), distortions in the form of twists can be observed in the molecular orientation (Figure 2b subset). This transition was previously studied and reported by Freedricksz[27]. The critical field is shown to be[28]:

$$H_C = \frac{\pi}{d}\sqrt{\frac{K_{22}}{\chi_a}} \tag{1}$$

Here, K_{22} represents the twist elastic constant, χ_a is the anisotropy in the diamagnetic susceptibility per volume, and H_c is the critical magnetic field. When $H \gg H_c$, the director orientation is defined by the orientation of the magnetic field. In the case of weak anchoring effects at the walls, the equation must be modified by adding a surface term[2].

The competition between the external magnetic field and the anchoring effect of walls and voxel surfaces is characterized in terms of equilibrium between the torques that they impose on the director. Based on this, De Gennes[2] introduced the concept of "magnetic coherence length" (ξ) to describe. This parameter can be computed as:

$$\xi = \frac{1}{H}\sqrt{\frac{K_{22}}{\chi_a}} \tag{2}$$

The value of ξ reflects the thickness of the transition region over which the director rotates. For most LCs, the magnetic coherence length is in the order of a few microns, assuming a magnetic flux density of 0.1-1 Tesla. Thus, for voxel dimensions (d) in the macroscopic scales ($d \gg \xi$), ξ becomes negligible and the molecular alignment is primarily governed by the orientation of the external magnetic field.

Elastic constants characterizing the nematic state can be calculated indirectly by measuring the critical field[29–31]. Once the magnetic anisotropy χ_a is measured separately[32], the elastic constant can be calculated by using the equation 1. Figure 2a illustrates the experimental setup used for critical field measurements. The sample was subjected to a magnetic field and the transition to the ordered state was detected through observation of a sudden change in the intensity of the transmitted light between crossed polarizers (Figure 2b). Table 1 shows different compositions that were explored with the goal of optimizing the crosslinking density to create an elastomer, while retaining the ability for magnetic alignment. In order to study the magnetic-induced alignment mechanism and compare the influence of each component in more detail, the critical magnetic fields (H_C) were measured as a function of thiol chain extenders, CTA, and mesogen concentration (Figure S2 in Supplementary Information†). The measurements were conducted within a temperature range of nematic phase stability. As we also observed before, a temperature window ($0.7T_{NI} - 0.9T_{NI}$) exists for orienting the mesogenic monomers. However, we found that the specific temperature value within this range had a negligible effect on the magnetic threshold. Therefore, further studies to measure H_C as a function of temperature were not necessary. Compositions containing thiol chain extenders (BDMT) required a higher amount of BHT thermal inhibitor to prevent thermal polymerization during measurements.

To compare the various compositions (Table 1), we calculated the $\frac{K_{22}}{\chi_a}$ ratio (twist elastic constant over magnetic susceptibility) using Equation 1. The values are shown in Table 2. This ratio provides insight into the correlation between composition and diamagnetic anisotropy. To decrease the crosslinking density, we added 3 wt% TBM to the RM composition (Table 1), resulting in RMC3. Interestingly, RMC3 showed only a minor change in $\frac{K_{22}}{\chi_a}$ ratio compared to RM, demonstrating that TBM is a useful component for achieving alignment using a magnetic field. We increased the amount of the chain extender BDMT until we achieved surface-induced alignment, which is necessary to meet the conditions for critical field measurements. However, we found that the addition of 10% wt BDMT alone did not result in optically clear samples, where the magnetic field can be used to drive uniaxial alignment. However, by adding 3% TBM to the composition containing 10% wt BDMT, we were able to regain uniaxial alignment. In contrast to the TBM effect, the concentration of the chain extender (BDMT) demonstrated remarkable control

on the elastic constant ($\frac{K_{22}}{\chi_a}$) (changed by 60% for RMT10C3 in comparison to RMC3). Similarly, the incorporation of the azobenzene dye to the network (RMZ4T10C composition) also increased the threshold magnetic field (lowering the magnetic susceptibility and increasing the elastic constant).

Table 2 Influence of the materials composition (chain transfer agent, chain extender, and azobenzene) on the ratio of the twist elastic constant to the magnetic susceptibility of the composition.

	RM	RMC3	RMT10C3	RMZ4T10C3
$\frac{K_{22}}{\chi_a}(A^2)$	2.18	2.24	3.58	4.23

The effect of the composition of the mesogenic inks on the properties of materials resulting from their photopolymerization was studied. We initially characterized the thermomechanical properties by measuring the shrinkage strain of uniaxially aligned LCE films as a function of temperature. LCEs contract along their director as a result of thermally induced order-disorder transitions. LCE films were fabricated by infiltrating monomer into PDMS-PDMS cells with a 50 μm gap. The mixture was polymerized by UV light after an external 300 mT magnetic field was applied in the nematic phase (75 °C). The compositions studied here obviate the need for an oligomerization step[4]. Figure 2c illustrates the average thermal strain for three cycles (cycles 2, 3, and 4) for each composition. The RMT10C3 sample showed up to 30% reversible shrinkage strain (Figure S4), which is significantly higher than the strain of glassy materials (3% for RM). This high shrinkage strain is mainly due to the presence of BDMT, as the inclusion of only TBM (RMC3) did not increase the shrinkage strain beyond 10%. To determine the phase transition temperatures of the unpolymerized mixture, we conducted differential scanning calorimetry (DSC) measurements for the compositions in the form of powder mixtures. The T_{NI} values were also confirmed using polarized optical microscopy (POM). The results indicated that the inclusion of TBM had only minor effects, while the phase transition temperatures (T_g and T_{NI}) decreased significantly after adding BDMT (Figure S5). To further characterize the thermomechanical properties as a function of monomer structure, we utilized dynamic mechanical analysis (DMA) to measure storage modulus (E′) and phase lag (Tan δ). From Figure 2d and e, it can be seen that the BDMT component played the main role in enhancing material softness.

In summary, we have demonstrated that the addition of TBM and BDMT to the LCE mixture can effectively tune the material properties, while preserving the ability to achieve alignment of the mesophases using a weak magnetic field. Among the compositions studied, RMT10C3 demonstrated excellent properties for 3D printing of complex LCE structures, as it could be easily aligned by low-intensity magnetic fields and exhibited large strain shape changes (up to 30% shrinkage strain). With this promising material in hand, we next turned our attention to developing light-responsive LCEs.

Building on this, we shifted our focus to 3D printable, photoresponsive structures. Light provides unique advantages over other stimuli, such as scalability, parallelized actuation of multiple actuators using flood illumination and when needed, achieving precise spatiotemporal control. Optical setups, such as utilizing digital micromirror device (DMD)[33], can transfer photonic energy in the form of complex patterns without the need for physical connections. Additionally, concepts such as self-shading and self-regulation[34] can be easily exploited for soft robotics applications. To enable light-sensitive actuation, the composition was modified to include a diacrylate that contains azobenzene (Figure 1a). The composition was tailored for printing by including a free radical photoinitiator (1 wt % Irgacure 784) and a light-absorbing dye (0.1 wt % methyl red). The addition of the dye not only inhibited thermal polymerization but also decreased light scattering and increased printing resolution, making the use of BHT unnecessary.

Before fabricating complex structures, optimal printing parameters and conditions were identified, such as curing temperature, dwell time, exposure time, and exposure intensity. Subsequently, the photoactuation performance of the resulting printed materials was also characterized. The latter is particularly important to understand the design space for soft robotic applications, where practical manipulation profiles can be realized. To estimate the time required for each step of the printing process, we must understand and characterize the dynamic behavior of mesogenic orientation in response to the external magnetic field. This behavior can be divided into two main aspects: alignment rate and decay rate. The alignment rate indicates the time needed for the mesogens to reorient parallel to the applied magnetic field. It is dependent on the twist viscosity, elastic constant, and the applied magnetic field strength. This rate informs the necessary dwell time before light exposure. On the other hand, the decay rate corresponds to the distortion of the magnetically-aligned mesogens once the external magnetic field is removed. The decay rate is independent of the external field value H, but it varies with composition and cell thickness[28]. The same critical field setup was used for the decay rate measurements to characterize the dynamics of loss of alignment when the mesogenic inks were removed from the magnetic field. The decay rate of $\sim$ 35 seconds was observed, as illustrated in Figure S6. This data can be helpful for future works in which the samples need to be transferred outside the magnetic field for further polymerization. However, this data is not sufficient to estimate the dwell time that is required to achieve the desired alignment in a magnetic field. In-situ polarized optical microscopy (POM) observation of the evolution of the molecular order after 10 minutes at 65 °C under the influence of the 300 mT magnetic field is shown in Figure 3c. The boundary conditions are Fluorinated Ethylene Propylene (FEP) coating of the window with weak anchoring on the bottom and elvamide with strong anchoring on the top, rubbed in a direction perpendicular to the magnetic field. It can be seen that optically clear LC monomer with the same molecular alignment is obtained after 10 minutes, which is higher than the required dwell time (5 minutes) for glassy materials[13], resulting from the higher elastic constant (and probably twist viscosity) of the LCE composition. In addition, this long dwell time necessitates thermal inhibitors to avoid unintended thermal polymerization.

While in the previous work the resolution of the voxels was 50 μm $\times$ 50 μm $\times$ 50 μm[13], this research focused on the structural refinement. Resolutions of 8 μm $\times$ 8 μm $\times$ 8 μm were made

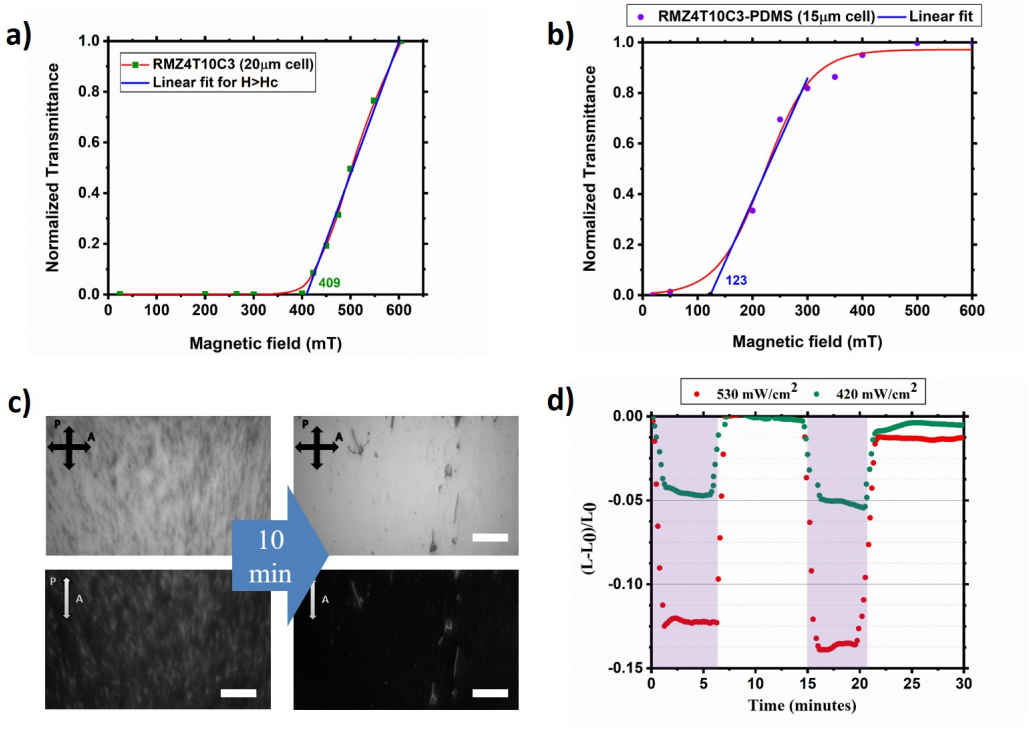

Fig. 3 a) Critical field measurement for RMZ4T10C3 mixture in a 20 μm cell at 65 °C. b) Measuring critical field (H_C) for RMZ4T10C3 composition with weak anchoring on one wall (PDMS coating) and strong anchoring on the other (rubbed elvamide). c) In-situ POM images of LC monomer mixture right after being fed to the printer compared to after 10 minutes dwell time (magnetic field $\perp$ surface induced alignment). d) Mechanical response of the printed uniaxially aligned LCE to UV light at two different intensities (420 mW/cm^2 & 530 mW/cm^2). Repeatable shape changes of up to 10% in response were observed.

possible using focusing optics. At this scale, we need to take into account the influence of surface anchoring and magnetic coherence length (ξ). Surface anchoring is particularly important when the thickness of the film is of the order of the coherence length. For the case of walls with weak anchoring effects, the equation 1 needs to be modified by adding the surface term[2]:

$$H_C = \frac{\pi}{d + 2l_e}\left(\frac{K_{22}}{\chi_a}\right)^{1/2} \tag{3}$$

where

$$l_e = \frac{K_{22}}{W} \tag{4}$$

W is the surface anchoring strength. For strong anchoring $W \to \infty$. For the current printer configuration, the lateral resolution (in XY plane) can be divided into three categories depending on the boundary conditions of the voxel:

1. No adjacent voxel is cured:
   In this case, no surface anchoring exists, and the dimensions of the voxel are dictated solely by the resolution of the DMD system, which is 8 μm.

2. One adjacent voxels is cured:
   The polymerized LCE has a strong anchoring and can affect the mesogens alignment of the mesogens. Assuming that the splay and bend elastic constants have approximately the same values as the twist elastic constant, the lateral resolution can be estimated using the following:

$$L_{min} = \xi = \frac{1}{H}\left(\frac{K_{22}}{\chi_a}\right)^{1/2} = \frac{\mu}{B}\left(\frac{K_{22}}{\chi_a}\right)^{1/2} \tag{5}$$

   Based on the data from Table 2, L_{min} was calculated to be approximately 8.6 μm.

3. When polymerized voxels constitute adjacent walls

   When both walls are polymerized, the anchoring effect is strong on both sides, similar to the critical field measurement conditions. Using equations 1 and 2, it can be shown that at critical field ($H = H_C$), the magnetic coherence length can be derived from $\xi = \frac{d}{\pi}$[2]. The minimum width can be calculated using the following equation:

$$L_{min} = \pi\xi = \frac{\pi}{H}\left(\frac{K_{22}}{\chi_a}\right)^{1/2} = \pi\frac{\mu}{B}\left(\frac{K_{22}}{\chi_a}\right)^{1/2} \tag{6}$$

   After substituting the values from Table 3 and using $B = 0.3$ T, we obtain $L_{min} \approx 27$ μm.

Resolution in the depth (Z) is slightly a different case, as it is governed by the platform (or previous printed layer) position or the material composition and the photonic energy of the exposure light, rather than the DMD system. From the molecular alignment point of view, there is always a weak surface anchoring condition in the bottom surface of the voxel (due to FEP or PDMS), and strong anchoring from the Elvamide (or printed material) surface. Instead of measuring the surface anchoring for the FEP or

PDMS materials directly, the critical field was measured for the LC monomer that was sandwiched between PDMS (weak anchoring) and rubbed elvamide (strong anchoring), resembling the 3D printing case. Based on the critical field value (H_C) measured from this, we can derive the resolution from the following:

$$Z_{min} = \pi\xi = \frac{H_C \times d}{H} = \frac{130.5 \times 15}{300} \approx 6.15\ \mu m \tag{7}$$

These results are summarized in Table 3. This data enabls a pathway for high resolution 3D printing of LCE using magnetically assisted stereolithography.

Table 3 Minimum dimensions of a voxel of material to obtain fully independent voxelated alignment using an external 300 mT magnetic field.

	XY (case 1)	XY (case 2)	XY (case 3)	Z
Minimum dimension [μm]	8	9	27	6.15

In addition to achieving magnetically-driven alignment of mesogens within the voxel, another crucial factor is the polymerization depth, which determines the resolution of the voxel normal to the build-plate. In cases where the structure has overhanging features, the depth is not simply the gap between the window and the previously printed layer (or build plate for the first layer). Instead, the polymerization depth is determined by the interplay of the energy dose of the light, the optical properties of the composition (including absorption coefficient and scattering effects), and the photonic energy threshold required to initiate polymerization[35]. For the composition developed in this work, we plotted the polymerization depth (or minimum thickness) as a function of photonic energy dosage (Figure S7), which we refer to as the "working curve". This curve was used to determine the required intensity of the polymerization light to achieve the desired thickness.

Having established the printing process parameters and conditions, we investigated the photomechanical responses of LCE printed using this method. A rectangular LCE strip with a thickness of 50 μm (single layer) and dimensions of 6 cm $\times$ 4 cm was printed. The mesogens were aligned in a monodomain configuration along the length by applying the magnetic field. After developing the sample, it was mounted vertically and a 10 mg weight was hanged from its lower end. Once the sample was exposed to UV light, it contracted along its length due to a decrease in the order parameter, lifting the 10 mg weight. Upon turning off the UV light source, the sample relaxed toward its original shape, lowering the weight. We repeated this experiment for three cycles and for two different intensities (420 mW/cm^2 & 530 mW/cm^2). We observed that the first cycles are not fully reversible (1.5% for 420 mW/cm^2 and 8% residual for 530 mW/cm^2). This mechanical hysteresis effect was reported in previous work of other research groups[36], is mostly caused by the lack of complete crosslinking during the polymerization step or by incomplete cis isomerization once the light is turned off. The latter can be circumvented through long blue light illumination. Despite the hysteresis effect, the sequential actuation mostly stabilized after the first cycle and the mechanical deformations were mostly repeatable. Figure 3d shows the next repeatable cycles. Photothermal effect likely played a role in these experiments, in addition to the actuation via photochromism of azobenzene. For the case of the lower intensity (420 mW/cm^2), the light energy increased the temperature up to 85°C, which resulted in a $\sim$ 1.7% contraction (Figure S8). Hence, the photoisomerization likely dominated the mechanical deformation for this intensity ($\sim$ 5% repeatable strain). At the higher intensity (530 mW/cm^2), much higher deformations were generated ($\sim$ 10% repeatable strain) due to the significant increase in photothermal effect compared to the lower intensity ($\sim$ 3.2% thermal strain at 100 °C). Based on the results, we achieved much higher photogenerated actuations with this newly developed LCE, with strain values of $5-10\%$, compared to glassy materials (which typically exhibit $\sim$ 1% strain)[37].

To further demonstrate the versatility of this platform using the newly developed material (RMZ4T10C3), we printed multiple light responsive LCE structures. First, a 50 μm thick ring with a complex molecular orientation (an annular section of a -1 topological defect) was printed. The ring is fabricated in 8 equal segments and 4 different orientations. While Figure 4a shows the alignment of each segment (blue rods) encoded by the external magnetic field direction, there are approximately 8.6 μm transition regions (twisting by 45 degrees) between each pair of segments, as based on the equations 2 and 5. Since the sample was photopolymerized at elevated temperatures (65 °C), it was deformed into a 3D shape after development and peeling due to anisotropic thermal expansion[38]. The ring demonstrated highly repeatable shape change in response to 530 mW/cm^2 UV light. The next sample is a gripper-like structure with three fingers. Due to the active monodomain alignment of the fingers, they can bend reversibly in response to UV exposure (Figure 4b).

The photomechanical deformation of our 3D printed structures are captured using a full-3D Finite Element (FE) simulations developed in COMSOL. As shown in Figure 4, the model could capture the shape changes with good accuracy. This FE model could be used further to systematically guide the design process of more complex structures.

Design and development of miniature flying robots has recently been studied by researchers using inspirations from nature such as flying insects or small birds. Piezoactuator driven wings remains the most commonly applied method to generate mechanical propulsion at this scale[39,40]. However, delivering the required energy (utilizing wires that tether the robot to the power supply, on-board battery, or photovoltaic array) to the actuator and integrating the control system remain the major challenges due to the weight limitation of the flying devices[41,42]. This can even make the flying impractical when scaled down to a few centimeters. Light-weight LCE actuators on the other hand can be activated and controlled remotely by light with spatiotemporal selectivity. However, research to date has not yet demonstrated any LCE applications for this field. Rogers and coworkers[43] studied free-falling seeds and then designed and manufactured a bio-inspired

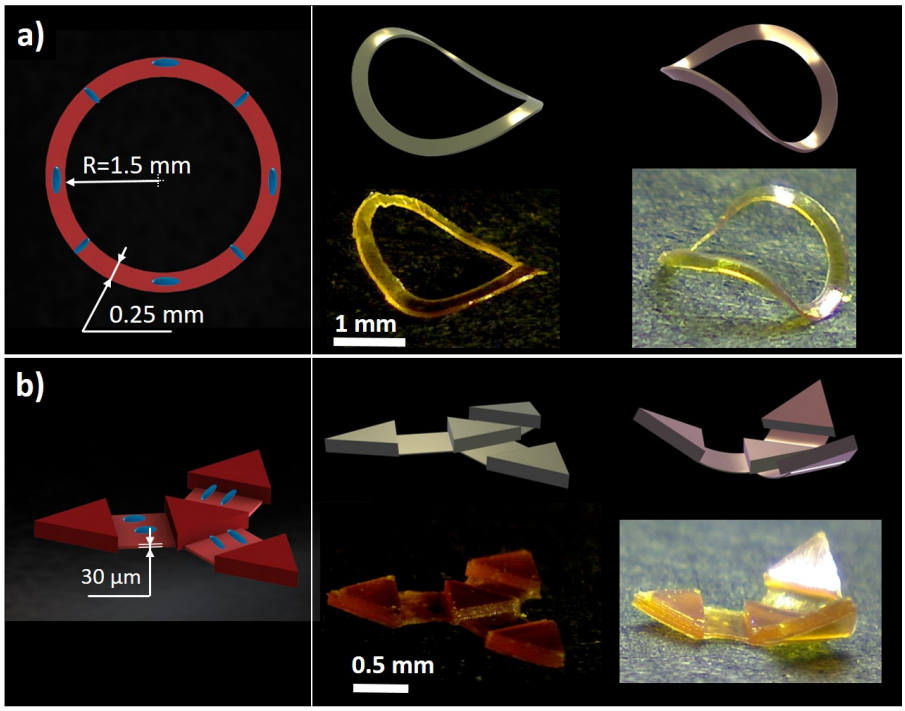

Fig. 4 3D printed structures with controlled and reversible shape morphing in response to UV light. The top figures illustrate the simulation data. a) A ring that represents an annular section of the -1 topological defect. b) Gripper-like structure.

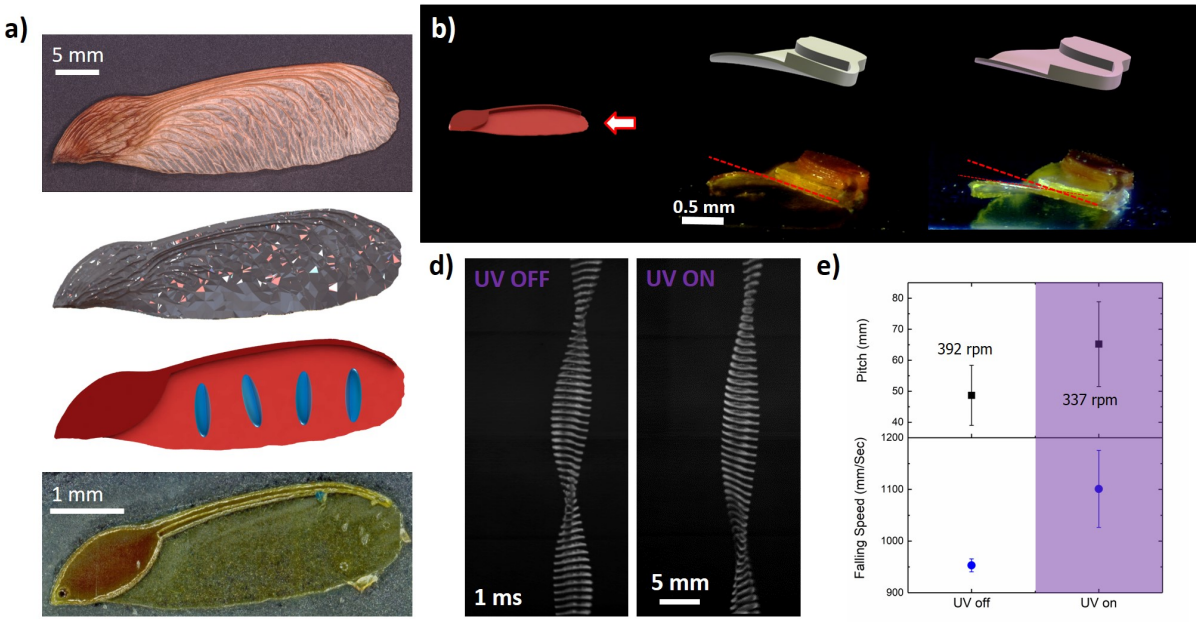

Fig. 5 Tuning the flight dynamics of the LCE microflier inspired by autorotating maple seeds. a) Design and fabrication of the LCE microflier through reverse-engineering of a maple seed. b) Change in the seed profile in response to UV irradiation (see also Movie S1). c) Tracking the autorotating free-flight path of the printed seed (in the presence and absence of UV irradiation). The images were generated by time stacking images with 1 ms intervals. d) Increase in average falling speed (15.5% increase) and average pitch distance (34% increase) as the result of UV light exposure. For each case, 5 trials were implemented.

3D microflier with enhanced levels of performance (high drag forces and low terminal velocities) during the fall. Novel applications such as environmental monitoring (e.g. fine dust pollution) were further proposed and illustrated through the integration of battery-free colorimetric sensors. However, the passive fliers were not adaptable mid-flight, once deployed.

Maple (Acer) samara fruits (containing the seeds), like many other wind-dispersed species, possess efficient aerodynamic characteristics that enable them to travel considerable distances[44]. This can be attributed to high lift forces generated through the auto-rotation of the seeds as they descend. 3D measurements of the flow around a dynamically scaled model of the maple seed revealed that the "angles of attack" (angle between the seed's reference line and the flow direction or more accurately $\alpha = \arctan(V_d/V_h)$, where V_d is descent speed and V_h is horizontal speed) and wing shape play the major roles in generation of the lift force[45]. As a result, the aerodynamic efficacy of the seed can be tuned by varying the angles of attack. Inspired by this flight mechanism and the potential to control the flight dynamics through the shape change, a regular maple seed (Figure 5a) was scanned at different angles by the optical profilometer (VR-3200, Keyence) and then the 3D data was merged into a single 3D geometry using Geomagic (3D Systems). This 3D shape (reverse-engineered data) was later used to design our microflier in Solidworks (Dassault Systems). To mimic the heavy seed and the leading edge of the samara's wing, the same regions were designed with higher thickness (150 μm). Figure 5a illustrates the steps that were taken to design and print the microflier inspired by a real maple samara. The molecular orientation was programmed in a way that the angle of attack and the profile change as a result of UV irradiation (Figure 5b and Movie S1). The mechanical deformation was limited to the thinner area (25 μm thick) while the leading edge and the core maintained their original shape due to their rigidity. To study the change in the flight dynamics of the samara mimicking LCE microflier in response to UV light, we utilized a simple setup (Figure S9) to drop it from the same location multiple times and monitor the fall by a high-speed video camera at 5000 fps rate. The videos were captured at 25 cm distance from the dropping point, where its rotating movement is more stable without much deviation to the sides. For the case of "UV on", the microflier was dropped after being exposed to 530 mW/cm^2 UV exposure for 1 minute. Each case was repeated 5 times to ensure the reliability and repeatability of the data. The results (Figures 5c and d) verified that UV light can be used to control the flight dynamics of the microflier. The falling speed and pitch length increased by 15.5% and 34% respectively. Basically, the microflier demonstrated more non-rotating behavior and less lift generation in the presence of the UV due to the change in its profile shape and decline of the angle of attack. The considerable variation of the data for the case of "UV on" can be explained by non-uniform relaxation of the microflier as it was moving away from the UV source in addition to less flight stability. This proposed microflier benefits from a simple and remote controlling method, UV lamp, without the need to expose the light at a certain angle. We can further take advantage of the light as the power source to irradiate the microflier at different frequencies and with more spatiotemporal selectivity. We can envision a swarm of these microfliers that are dispersed over an area and their flying behavior is selectively and locally controlled by the light. Sensor integration for the purpose of data collection, as discussed by Kim et al., can further broaden the applications of these structures[43]. This example illustrates the capability unlocked by the combination of the 3D printing configuration, which allowed us to harness biomimetic motions to realize passive fliers, whose performance can be adapted mid-flight.

3 Conclusions

Use of chain transfer agents in liquid crystalline inks was found to result in the preservation of the ability to program the director in a voxelated fashion using the interplay of superposed magnetic fields and spatially-selective polymerization. The ability to modulate the macromolecular structure of printed parts and their subsequent coupling to actinic stimuli offers a framework to voxelate and compose non-trivial structural and functional responses. Complex, active structures with refined structural features become feasible. This platform offers orthogonal control over the molecular order using externally applied magnetic fields, which decouples the molecular ordering from the geometry, build path, process conditions, and boundary conditions. This method enables the development of LCE structures with tailored mechanical, optical, and sensing properties, which can find various applications in soft robotics, microfluidics, and biomedical engineering. The fabricated structures, including a light-responsive gripper and a topological defect, demonstrated the potential of this method for creating functional LCE devices. Furthermore, we demonstrated a bioinspired LCE microflier that can be remotely controlled using UV light, without the need for wires or batteries. This microflier design takes inspiration from the aerodynamic properties of maple seeds, and can potentially find use in environmental monitoring or as a soft robot that can be precisely deployed.

4 Materials and methods

4.1 Materials

This study explored a LCE system based on a diacrylate mesogen RM82 ((1,4-bis-[4-(6-acryloyloxhexyloxy) benzoyloxy]-2 methylbenzene, Wilshire Technologies). The chain transfer agent used was Tetrabromomethane (TBM) from Sigma-Aldrich, while the chain extender was 1,4 benzenedimethanethiol (BDMT) purchased from the same supplier. For the UV range photoinitiator, we used Iragcure 819 from Ciba Specialty Chemicals, while BHT (2,6-Di-tert-butyl-4-methylphenol) was used to inhibit thermal polymerization. We also utilized Irgacure 784 from Ciba Specialty Chemicals as the photoinitiator for visible light wavelength. The azobenzene dye, azo 6c (4,4'-di(6-(acryloxy)hexyloxy)azobenzene), was incorporated into the composite for photoresponsive properties. Methyl red (2-(4-Dimethylaminophenylazo)benzoic acid, 4-Dimethylaminoazobenzene-2′-carboxylic acid, Acid Red 2 purchased from Sigma-Aldrich) served as the light absorber. Finally, we used PDMS (Sylgard 184 Dow Corning 184 Silicone Elas-

tomer) and optically clear Polytetrafluoroethylene (PTFE) silicone adhesive tape (7562A32, McMaster-Carr) to make substrates with low surface anchoring.

4.2 Critical field measurements

For critical field measurement experiments, cells with 15 μm gaps were made by gluing glasses with indium tin oxide (ITO) coating (06478B-AB, SPI Supplies) and 10 mm $\times$ 10 mm coverslips, utilizing spacers (15μm silica microspheres) between them. After cleaning the coverslips and glasses through sonication in isopropyl alcohol (IPA) and plasma cleaning, they were spin-coated with Elvamide (DuPont). After 10 minutes of baking at 80 °C, they were rubbed with a velvet cloth to impose surface alignment. Once the cell was assembled, the melted monomer mixture was added and infiltrated the cell at the isotropic temperature. Then the cell was cooled down, the gaps were sealed using epoxy glue, and the wires were connected by applying conductive epoxy or soldering. The uniaxial molecular orientation was checked at the nematic phase using crossed polarizers. The sample needs to be perfectly transparent as any defect can affect the measurements of the transmitted light. Next, the cell was mounted between two crossed polarizers, in a way that the molecular alignment (rubbing direction) was vertical. The exposed light from a He-Ne laser ($\lambda = 633$ nm, HNL050L, Thorlabs) transmitted through the polarizers, cell, and a Soleil-Babinet Compensator (SBC-VIS, Thorlabs). The transmitted light power was captured by a highly sensitive photodiode power sensor (S120C, Thorlabs). Two permanent neodymium magnets (K&J Magnetics) were mounted on a linear stage (59-337, Edmund Optics) to apply a wide range (20-680 mT in the center) of external magnetic fields (perpendicular to the rubbing direction, as depicted in Figure 2a) by adjusting their distance to each other. A Teslameter (SDL900, Instrumart) was used to track the magnetic flux density. To control the cell temperature, an Arduino PID controlling system and a self-adhesive thermocouple (SA3-K, Omega) was connected to the cell. The measurements were executed at a certain temperature (nematic phase) rather than going through a N-ISO thermal cycle for each data point. To study the magnetic orientation mechanism and determine the critical field, the intensity of the transmitted light was measured as a function of the magnetic field (magnetic flux density). The kinetic effect was eliminated by executing the measurement after the data was stabilized (generally after 10-20 minutes) at each point. After the threshold, a sudden change could be observed that indicated the change in the molecular alignment (twisting in this case) as the magnetic field started to overcome the surface anchoring effect[46]. Sigmoid functions were used to fit a curvature to the data. Finally, the critical field was estimated by a linear fit. The accuracy of the setup was confirmed by measuring the critical field for E7 material at room temperature (Figure S3). The result (574 mT for 14μm thick cell) demonstrated good agreement ($\sim 1\%$ error) with the reported data in Ref.[32,46]. Based on the critical field values we were able to calculate the required magnetic field and De Gennes's magnetic coherence length[2] for different compositions and surfaces.

4.3 Characterization

The composition thermal properties such as glass transition temperature (T_g) are collected using differential scanning calorimetry (DSC, Perkin Elmer Diamond). The sample heat flow and the reference heat flow are compared as a function of temperature to detect thermal transitions. The nematic-isotropic phase transition temperature (T_{NI}) was also identified using polarized imaging.

The viscoelastic behavior of the LCE films can be studied using a dynamic mechanical analyzer (DMA, Perkin Elmer 8000). Rectangular samples are clamped to the device and sinusoidal forces are applied, capturing the stress and strain as a function of temperature. Important mechanical properties such as storage modulus, loss modulus, and phase angle can be determined from the data.

To measure the contractile strain in response to heat stimuli, rectangular pieces were cut and placed on a hotplate with a temperature controller. Silicone oil was added to decrease the friction and a thin coverslip was placed on top of the sample to restrict the the deformation to in-plane shrinkage. Two thermocouples (5SRTC-TT-J-30-36, Omega) and a thermometer (HH802U, Omega) were used to measure the temperature. Images and videos were captured by Aven Mighty Scope 1.3M USB Digital Microscope cameras (20-200x magnification, 7 frames/s rate). The shrinkage strain as a function of temperature was calculated using an open-source video analysis software[47] that can track the displacement. The strain values as a function of temperature were generally plotted by calculating the average values from cycles 2,3, and 4 (the first cycle was not perfectly repeatable).

Photoactuation characterizations were executed by utilizing a UV LED lamp (OmniCure AC450, Lumen Dynamics) to irradiate unpolarized UV light up to 520 mW/cm^2 intensity. The photostrain values were calculated from the curvature of the film that was held by a tweezer in front of the UV lamp, or from performing photoactuation experiments where the film lifted a 10 mg weight against gravity.

PHANTOM V2511 High-Speed Video Camera was used to capture images at high speed (5000 fps). For higher magnification imaging Smartzoom(5 Digital Microscope, ZEISS) was used. Another useful tool is an optical profilometer (VR-3200, Keyence) which could provide 3D data of the surface.

4.4 Printing method

The printing procedure followed the procedure reported in Ref.[13] To prevent the sticking of the printed layer to the window caused by the presence of the BDMT thiol in the new LCE composition, the Polydimethylsiloxane (PDMS) coating used in the previous work is no longer effective in preventing adhesion. This is due to the reduction in the oxygen inhibition effect[48]. As a result, optically clear FEP tape was used on the window instead.

For the final development, the sample was immersed in the Propylene glycol monomethyl ether acetate (PGMEA, Sigma-Aldrich) for 20 minutes, followed by sonication in IPA for 5 minutes. The sample was dried by placing it in vacuum for 2-3 min. To complete the conversion of monomers, the printed samples were post-cured through exposure to $\sim$ 20 mW/cm^2 UV light.

However, samples functionalized with azobenzene were cured using green light for about 30 minutes and heating the sample up to 75 °C for 1 hour.

The setup is equipped with an imaging system (DCC3260M and M730L5, Thorlabs) for in-situ polarized optical microscopy (Figure S10). This provides the empowerment to study the change of the molecular order as a function of composition, magnetic field intensity, temperature, and time inside the 3D printer.

4.5 Modeling and simulation

A nonlinear finite element (FE) analysis was conducted using a commercial solver, COMSOL Multiphysics (Version 5.6). The 3D-printed liquid crystal polymer structures are modeled as full 3D structures. The initial nematic alignments in the structures are represented using rotated local coordinate systems. The rotated systems match the printed molecular orientations in each section of the structure. The material properties, governing equations, and boundary conditions are defined using the Solid Mechanics module in the software. The Young's Modulus of the material is defined as a temperature-dependent function, extracted from the DMA data (Figure 2d). Externally-induced strain in the system is built using two components, the thermal- and photo-induced strains. The thermally-induced strain is defined as a temperature-dependent function using the thermal strain tests shown in Figure 2c and is assumed to act uniformly through the thickness of the films. The photo-induced strains are determined using the mechanical response of the sample exposed to UV light (Figure 3d) and the temporal temperature due to UV light radiation (Figure S8 in Supplementary Information†). Unlike the thermal strains, the photo strains are defined to have an exponential distribution following Beer's law through the thickness of the film with the surface facing the lamp receiving the maximum effect[49]. The spontaneous strain (combination of thermal and photo strains) is considered diagonal along the principal frame of the LCP, defined by the nematic director. The strain in the transverse plane is specified so that the material deforms at constant volume throughout the actuation[50]. To solve the quasi-static model, we used an Iterative Newton's method with a variable damping factor. The load ramping approach (Auxiliary Sweep) is implemented through a parameter t, representing time, to ensure the convergence of the problem.

Conflicts of interest

There are no conflicts to declare.

Acknowledgements

Support from the National Science Foundation (1921842, 2147830 and 2147703) is acknowledged.

Notes and references

1 K. Bhattacharya and R. D. James, *science*, 2005, **307**, 53–54.
2 P.-G. De Gennes and J. Prost, *The physics of liquid crystals*, Oxford university press, 1993, vol. 83.
3 T. H. Ware, M. E. McConney, J. J. Wie, V. P. Tondiglia and T. J. White, *Science*, 2015, **347**, 982–984.
4 C. P. Ambulo, J. J. Burroughs, J. M. Boothby, H. Kim, M. R. Shankar and T. H. Ware, *ACS applied materials & interfaces*, 2017, **9**, 37332–37339.
5 A. Kotikian, R. L. Truby, J. W. Boley, T. J. White and J. A. Lewis, *Advanced Materials*, 2018, **30**, 1706164.
6 M. López-Valdeolivas, D. Liu, D. J. Broer and C. Sánchez-Somolinos, *Macromolecular rapid communications*, 2018, **39**, 1700710.
7 A. Kotikian, C. McMahan, E. C. Davidson, J. M. Muhammad, R. D. Weeks, C. Daraio and J. A. Lewis, *Science Robotics*, 2019, **4**, eaax7044.
8 C. P. Ambulo, M. J. Ford, K. Searles, C. Majidi and T. H. Ware, *ACS applied materials & interfaces*, 2020, **13**, 12805–12813.
9 A. Kotikian, J. M. Morales, A. Lu, J. Mueller, Z. S. Davidson, J. W. Boley and J. A. Lewis, *Advanced Materials*, 2021, **33**, 2101814.
10 S. Gantenbein, K. Masania, W. Woigk, J. P. Sesseg, T. A. Tervoort and A. R. Studart, *Nature*, 2018, **561**, 226–230.
11 M. O. Saed, C. P. Ambulo, H. Kim, R. De, V. Raval, K. Searles, D. A. Siddiqui, J. M. O. Cue, M. C. Stefan, M. R. Shankar *et al.*, *Advanced Functional Materials*, 2019, **29**, 1806412.
12 D. J. Roach, X. Kuang, C. Yuan, K. Chen and H. J. Qi, *Smart Materials and Structures*, 2018, **27**, 125011.
13 M. Tabrizi, T. H. Ware and M. R. Shankar, *ACS applied materials & interfaces*, 2019, **11**, 28236–28245.
14 A. Münchinger, V. Hahn, D. Beutel, S. Woska, J. Monti, C. Rockstuhl, E. Blasco and M. Wegener, *Advanced Materials Technologies*, 2022, **7**, 2100944.
15 M. Carlotti, O. Tricinci, F. den Hoed, S. Palagi and V. Mattoli, *Open Research Europe*, 2021, **1**, 129.
16 Y. Guo, H. Shahsavan and M. Sitti, *Advanced Materials*, 2020, **32**, 2002753.
17 Y. Guo, J. Zhang, W. Hu, M. T. A. Khan and M. Sitti, *Nature communications*, 2021, **12**, 1–9.
18 N. A. Traugutt, D. Mistry, C. Luo, K. Yu, Q. Ge and C. M. Yakacki, *Advanced Materials*, 2020, **32**, 2000797.
19 S. Li, H. Bai, Z. Liu, X. Zhang, C. Huang, L. W. Wiesner, M. Silberstein and R. F. Shepherd, *Science Advances*, 2021, **7**, eabg3677.
20 M. Fang, T. Liu, Y. Xu, B. Jin, N. Zheng, Y. Zhang, Q. Zhao, Z. Jia and T. Xie, *Advanced Materials*, 2021, **33**, 2105597.
21 B. Jin, J. Liu, Y. Shi, G. Chen, Q. Zhao and S. Yang, *Advanced Materials*, 2022, **34**, 2107855.
22 S. Schuhladen, F. Preller, R. Rix, S. Petsch, R. Zentel and H. Zappe, *Advanced materials*, 2014, **26**, 7247–7251.
23 N. P. Godman, B. A. Kowalski, A. D. Auguste, H. Koerner and T. J. White, *ACS Macro Letters*, 2017, **6**, 1290–1295.
24 H. J. Hutchins, *PhD thesis*, Aston University, 2021.
25 T. Furuncuoglu, I. Ugur, I. Degirmenci and V. Aviyente, *Macromolecules*, 2010, **43**, 1823–1835.
26 B. C. Whang, G. Lichti, R. G. Gilbert, D. H. Napper and D. F. Sangster, *Journal of Polymer Science: Polymer Letters Edition*, 1980, **18**, 711–716.

27 V. Fréedericksz and V. Zolina, *Transactions of the Faraday Society*, 1933, **29**, 919–930.
28 S. Chandrasekhar, *Liquid crystals*, Cambridge University Press, Cambridge [England];New York, NY, USA, 2nd edn, 1992, pp. 98–162.
29 P. R. Gerber and M. Schadt, *Zeitschrift für Naturforschung A*, 1980, **35**, 1036–1044.
30 H. Gruler, T. J. Scheffer and G. Meier, *Zeitschrift für Naturforschung A*, 1972, **27**, 966—-976.
31 N. Madhusudana and R. Pratibha, *MOL CRYST LIQ CRYST*, 1982, **89**, 249–257.
32 S.-T. Wu, W. H. Smith and A. M. Lackner, *Molecular Crystals and Liquid Crystals*, 1986, **140**, 83–93.
33 S. Palagi, A. G. Mark, S. Y. Reigh, K. Melde, T. Qiu, H. Zeng, C. Parmeggiani, D. Martella, A. Sanchez-Castillo, N. Kapernaum *et al.*, *Nature materials*, 2016, **15**, 647–653.
34 O. M. Wani, H. Zeng and A. Priimagi, *Nature communications*, 2017, **8**, 1–7.
35 P. F. Jacobs, *Rapid prototyping & manufacturing: fundamentals of stereolithography*, Society of Manufacturing Engineers, 1992.
36 L. Ceamanos, Z. Kahveci, M. López-Valdeolivas, D. Liu, D. J. Broer and C. Sánchez-Somolinos, *ACS Applied Materials & Interfaces*, 2020, **12**, 44195–44204.
37 C. Van Oosten, K. Harris, C. Bastiaansen and D. Broer, *The European Physical Journal E*, 2007, **23**, 329–336.
38 H. Zeng, O. M. Wani, P. Wasylczyk and A. Priimagi, *Macromolecular rapid communications*, 2018, **39**, 1700224.
39 D. Floreano and R. J. Wood, *nature*, 2015, **521**, 460–466.
40 E. Farrell Helbling and R. J. Wood, *Applied Mechanics Reviews*, 2018, **70**, year.
41 K. Y. Ma, P. Chirarattananon, S. B. Fuller and R. J. Wood, *Science*, 2013, **340**, 603–607.
42 N. T. Jafferis, E. F. Helbling, M. Karpelson and R. J. Wood, *Nature*, 2019, **570**, 491–495.
43 J. Rogers, B. H. Kim, K. Li, J.-T. Kim, Y. Park, H. Jang, X. Wang, Z. Xie, S. Won, W. J. Jang *et al.*, 2021.
44 R. Nathan, G. G. Katul, H. S. Horn, S. M. Thomas, R. Oren, R. Avissar, S. W. Pacala and S. A. Levin, *Nature*, 2002, **418**, 409–413.
45 D. Lentink, W. B. Dickson, J. L. Van Leeuwen and M. H. Dickinson, *Science*, 2009, **324**, 1438–1440.
46 H. Chen, R. Zhu, J. Zhu and S.-T. Wu, *Liquid Crystals*, 2015, **42**, 1738–1742.
47 *https://physlets.org/tracker/*, `https://physlets.org/tracker/`.
48 A. K. O'Brien, N. B. Cramer and C. N. Bowman, *Journal of Polymer Science Part A: Polymer Chemistry*, 2006, **44**, 2007–2014.
49 D. Corbett, C. L. van Oosten and M. Warner, *Phys. Rev. A*, 2008, **78**, 013823.
50 A. DeSimone and L. Teresi, *The European Physical Journal E*, 2009, **29**, 191–204.